Inorganic Chemistry

Article

pubs.acs.org/IC

Synthesis and Characterization of $MnCrO_4$, a New Mixed-Valence Antiferromagnet

Vladimir B. Nalbandyan,[†,*] Elena A. Zvereva,[‡] Galina E. Yalovega,[§] Igor L. Shukaev,[†] Anastasiya P. Ryzhakova,[†] Alexander A. Guda,[§] Alessandro Stroppa,[⊥] Silvia Picozzi,[⊥] Alexander N. Vasiliev,[‡,∥] and Myung-Hwan Whangbo[#]

[†]Chemistry Faculty, Southern Federal University, 7 ul. Zorge, Rostov-na-Donu, 344090 Russia

[‡]Faculty of Physics, Moscow State University, Moscow, 119991 Russia

[§]Faculty of Physics, Southern Federal University, 5 ul. Zorge, Rostov-na-Donu, 344090 Russia

[⊥]CNR-SPIN, L'Aquila, Italy

[#]Department of Chemistry, North Carolina State University, Raleigh, North Carolina 27695-8204, United States

[∥]Theoretical Physics and Applied Mathematics Department, Ural Federal University, 620002 Ekaterinburg, Russia

Supporting Information

ABSTRACT: A new orthorhombic phase, $MnCrO_4$, isostructural with $MCrO_4$ (M = Mg, Co, Ni, Cu, Cd) was prepared by evaporation of an aqueous solution, $(NH_4)_2Cr_2O_7$ + 2 $Mn(NO_3)_2$, followed by calcination at 400 °C. It is characterized by redox titration, Rietveld analysis of the X-ray diffraction pattern, Cr K edge and Mn K edge XANES, ESR, magnetic susceptibility, specific heat and resistivity measurements. In contrast to the high-pressure $MnCrO_4$ phase where both cations are octahedral, the new phase contains Cr in a tetrahedral environment suggesting the charge balance $Mn^{2+}Cr^{6+}O_4$. However, the positions of both X-ray absorption K edges, the bond lengths and the ESR data suggest the occurrence of some mixed-valence character in which the mean oxidation state of Mn is higher than 2 and that of Cr is lower than 6. Both the magnetic susceptibility and the specific heat data indicate an onset of a three-dimensional antiferromagnetic order at $T_N \approx 42$ K, which was confirmed also by calculating the spin exchange interactions on the basis of first principles density functional calculations. Dynamic magnetic studies (ESR) corroborate this scenario and indicate appreciable short-range correlations at temperatures far above T_N. $MnCrO_4$ is a semiconductor with activation energy of 0.27 eV; it loses oxygen on heating above 400 °C to form first Cr_2O_3 plus Mn_3O_4 and then $Mn_{1.5}Cr_{1.5}O_4$ spinel.

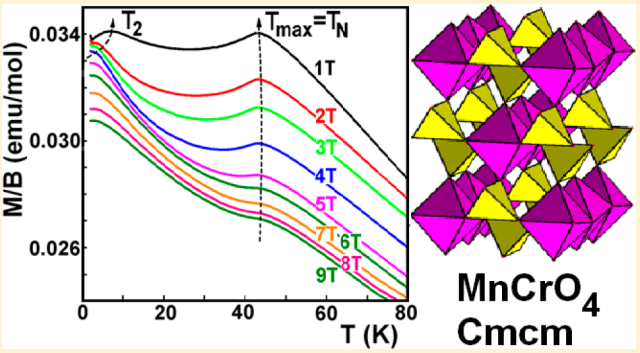

1. INTRODUCTION

Isostructural orthorhombic $M^{2+}CrO_4$ compounds are known for a long time for M = Mg,[1] Cd,[1] Ni,[1,2] Co,[2] Cu.[3,4] Those with magnetic ions, M = Ni, Co, and Cu, are quasi-one-dimensional antiferromagnets.[2,4] In $CuCrO_4$, a possible multiferroic behavior was discussed.[4] It would be very interesting to study properties of their analogues with higher spins, Fe^{2+} ($S = 2$) and Mn^{2+} ($S = 5/2$). A divalent iron is a strong reducing agent, which is obviously incompatible with such a strong oxidizer as chromate. This problem is less serious with Mn^{2+}, but Mn^{2+} chromates are unknown. The high-pressure $MnCrO_4$ has a distorted rutile-type structure with both cations in octahedral coordination and is believed to have the formulation $Cr^{3+}Mn^{5+}O_4$.[5] So far attempts to prepare and characterize the normal chromate, $Mn^{2+}Cr^{6+}O_4$, have been inconclusive. Campbell[6] reported an IR spectrum of black "$MnCrO_4$" that gave "no measurable X-ray diffraction pattern". "$MnCrO_4$" was tested as a photocatalyst,[7] but its origin, chemical or X-ray data were not specified. This phase is still absent in the Master Database of the ICDD's Powder Diffraction File (PDF), in contrast to the case of several spinel-type manganese chromium oxides (with the oxidation states of both metals not exceeding 3+) prepared by normal-pressure high-temperature reactions. Besides, a triclinically distorted ilmenite-type $MnCrO_3$ phase was obtained at high pressure.[8] Precipitation from aqueous solutions of $MnSO_4$ and K_2CrO_4 resulted in a dark brown product presumed to be $KMn_2(CrO_4)_2(OH)(H_2O)$.[9] Its rather weak powder X-ray pattern was not indexed. Besides magnetic properties, manganese chromium oxides attract attention as possible precursors for preparing Li-ion battery cathode materials such as $Li_{1.2}Cr_{0.4}Mn_{0.4}O_2$[10] or $Li(Cr_xMn_{1-x})O_2$.[11] In

Received: June 1, 2013

   dx.doi.org/10.1021/ic401391b | Inorg. Chem. XXXX, XXX, XXX−XXX

this paper, we report preparation and characterization of a new phase of $MnCrO_4$, a mixed-valence tetrahedral chromate.

2. EXPERIMENTAL SECTION

2.1. Preparation. First attempts to obtain $MnCrO_4$ from aqueous solutions of $MnSO_4$ and K_2CrO_4 in equimolar amounts led to a poorly crystallized precipitate whose powder pattern does not match that reported for $KMn_2(CrO_4)_2(OH)(H_2O)$[9] and cannot be indexed. Therefore, we decided to apply a combination of "wet" and "dry" preparation methods and avoid foreign components such as K^+ and SO_4^{2-} that cannot be eliminated by heat treatment. Starting materials were reagent-grade ammonium dichromate and manganese nitrate. The former can be easily dried. The latter is extremely hygroscopic so we use it in the form of concentrated aqueous solution. Weighed portions of this solution were carefully evaporated in porcelain crucibles, calcined at 750 °C and weighed again as Mn_2O_3. This provided a mass fraction of the salt in the solution. Weighed portions of this solution and ammonium dichromate were mixed in the [Mn]:[Cr] ratio of unity and evaporated under a flue while mixing thoroughly. The dry black residue was ground with a mortar and pestle and calcined at 400 °C for an hour with intermittent regrinding. The diamagnetic analogue, $InVO_4$, was prepared by solid-state reactions of In_2O_3 and V_2O_5 for 2 h at 650, 800, and 900 °C with intermediate regrinding and pressing. Its phase purity was confirmed against the PDF cards 00−48−898 and 01−71−1689.

2.2. Chemical Analysis. The [Mn]:[Cr] ratio was determined by the starting composition, and the oxygen content was analyzed by redox titration (see the Supporting Information for details). The major part of each sample dissolved for analysis quite rapidly leaving a small residue that remained undissolved even after prolonged heating. The presence of minor foreign phase(s) was confirmed by X-ray diffraction, see below. On the basis of the starting sample masses, average oxygen content per formula unit was calculated to be 3.86. However, taking into account the incomplete dissolution, the actual oxygen content should be higher, in reasonable accord with the expected stoichiometric formula. Hereafter, we shall assume composition to be $MnCrO_4$ as confirmed later by several independent techniques.

2.3. X-ray Diffraction and Absorption. An X-ray diffraction (XRD) study was performed in CuKα radiation using an ARL X'TRA diffractometer equipped with a solid state Si(Li) detector. For Rietveld refinements, GSAS+EXPGUI suite[12,13] was used.

X-ray absorption near-edge structure (XANES) spectra at the Mn and Cr K edges were measured with a laboratory Rigaku RXAS spectrometer in transmission mode using Ge (311) monochromator crystal with energy resolution 0.7 and 1.1 eV for chromium and manganese, respectively. An argon-filled proportional counter and a scintillation detector were used to record the intensity of the incident and transmitted X-rays, correspondingly. To decrease noise, ten scans were averaged for each sample. After background subtraction, the calibrated spectra were normalized.

2.4. Magnetic and Thermal Studies. Magnetic measurements were performed by means of a Quantum Design PPMS system. The temperature dependence of the magnetic susceptibility was measured at the magnetic field B = 0.1 T in the temperature range 2−350 K and under variation of the magnetic field up to B = 9 T in the temperature range 2−100 K. In addition, the isothermal magnetization curves were obtained in external fields up to 9 T at two temperatures (T = 2 and 5 K) after cooling the sample in zero magnetic field.

Heat capacity measurements were carried out by a relaxation method using a Quantum Design PPMS system. The plate-shaped samples of $MnCrO_4$ of ∼0.2 mm thickness and 12.2 mg mass and $InVO_4$ of ∼0.3 mm thickness and 25 mg mass were obtained by pressing of the polycrystalline powder. For both samples the data were collected at zero magnetic field in the temperature range 1.9−100 K.

Electron spin resonance (ESR) studies were carried out using an X-band ESR spectrometer CMS 8400 (ADANI) ($f \approx 9.4$ GHz, $B \leq 0.7$ T) equipped with a low temperature mount, operating in the range T = 5−300 K. The effective g-factor has been calculated with respect to a BDPA (a,g-bisdiphenyline-b-phenylallyl) reference sample with g_{et} = 2.00359.

3. RESULTS AND DISCUSSION

3.1. Crystal Structure of $MnCrO_4$. The XRD pattern of $MnCrO_4$ (Figure 1) was indexed by the ITO program in a C-centered orthorhombic cell with reasonable accuracy. Careful analysis revealed additional absences indicating a glide plane. Thus, by analogy with the known $MCrO_4$ compounds,[1−4] *Cmcm* might be selected as the most probable space group. The cubic root of the formula volume of the new compound, together with those for five previously known chromates, is in excellent linear relationship with the ionic radii (Figure 2, left),

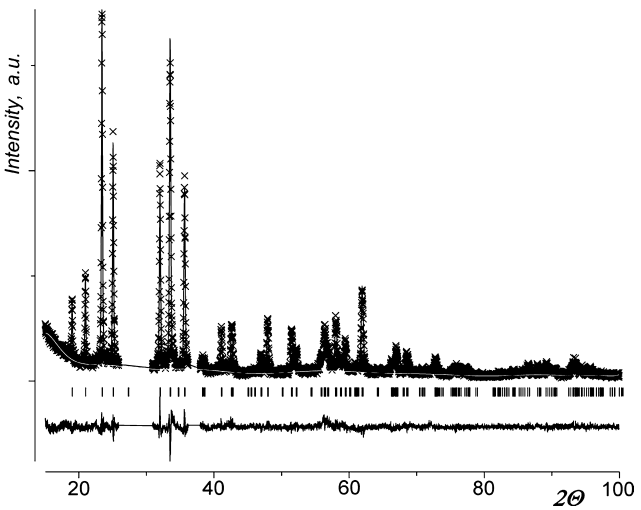

Figure 1. XRD pattern of $MnCrO_4$: Crosses, experimental data; line, calculated pattern; line at the bottom, difference profile; vertical bars, Bragg positions. Two regions containing impurity peaks (see Figure 3) were excluded.

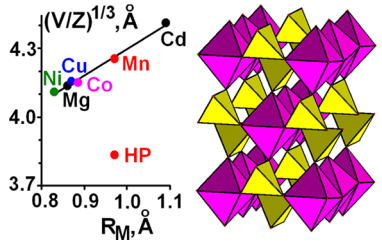

Figure 2. Correlation between the Shannon's[14] octahedral radii of M^{2+} and the reduced unit-cell parameters for $MCrO_4$ compounds,[1−4] $(V/Z)^{1/3}$ (left), and polyhedral view of the crystal structure of $MnCrO_4$ (right). Here, V is the unit-cell volume, Z is the number of formula units in the unit cell, and HP denotes the high-pressure form of $MnCrO_4$.[5]

thus confirming the structural analogy and the adopted composition. As evident from the plot, the formula volume of the new phase is much larger than that for the high-pressure form[5] because of the reduced coordination number of Cr.

Besides the strong and sharp indexed reflections, the XRD pattern contained several weak and diffuse reflections that could not be indexed. Trying to obtain a purer product, we repeated the synthesis to obtain exactly the same reflections from $MnCrO_4$ whereas most unindexed reflections disappeared but some new weak and diffuse peaks appeared (Figure 3). This

dx.doi.org/10.1021/ic401391b | Inorg. Chem. XXXX, XXX, XXX−XXX

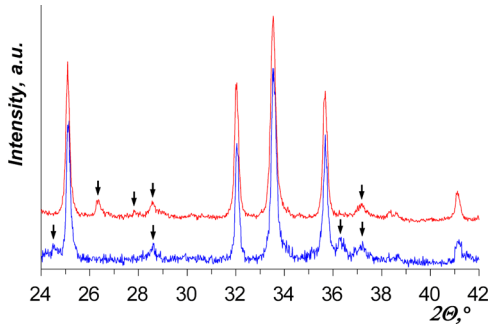

Figure 3. Partial XRD patterns of the two nominally identical $MnCrO_4$ preparations showing the strongest reflections from impurity phases, mostly irreproducible, indicated by arrows.

confirms that these unindexed reflections are from impurity phase(s) and not from $MnCrO_4$. The structure refinements carried out by using the whole pattern with no account for the impurities and by excluding the two corresponding angular ranges led essentially to the same results. Figure 1 shows the results from the second refinement and the corresponding crystallographic information file (cif) is given in the Supporting Information. Table 1 lists the unit cell data and refinement

Table 1. Crystallographic Data and Refinement Details of $MnCrO_4$

cryst syst	orthorhombic
space group	*Cmcm* (63)
a (Å)	5.5876(2)
b (Å)	8.4568(3)
c (Å)	6.5213(2)
V (Å^3)	308.15(2)
angular range (2Θ)	15−100°
no. of data points	4251
no. of params	46
R_p	0.0863
R_{wp}	0.1034
χ^2	1.519

Table 2. Interatomic Distances (in Å) and Bond Valence Sums (BVS) in $MnCrO_4$

	Mn	Cr	BVS
O1	2.110(5) × 2	1.662(5) × 2	1.85
O2	2.1723(3) × 4	1.671(5) × 2	2.10
BVS	2.26	5.64	

details, and Table 2, principal interatomic distances and bond valences. It is confirmed that $MnCrO_4$ is strictly isostructural with $MCrO_4$ (M = Mg, Co, Ni, Cu, Cd). A polyhedral view of the structure is represented in Figure 2 (right). The structure contains infinite [001] chains of edge-sharing MnO_6 octahedra connected in two other directions by chromium atoms in tetrahedral coordination, typical of chromates (6+). First steps of structure refinement were made with total isotropic U = 0.02 Å^2. Then, individual isotropic U values were introduced for all atom sorts and χ^2 dropped to 2.05. Finally, for the heavy atoms (Mn and Cr) anisotropic U_{ij} were refined. However, the resulting U_{ij} values do not show any sufficiently preferable direction of thermal vibrations.

3.2. Thermal Decomposition. At 700−1000 °C in air, the mixed oxide with [Mn]:[Cr] ratio of 1 crystallizes in the cubic spinel type, $Mn_{1.5}Cr_{1.5}O_4$.[5] Therefore, $MnCrO_4$ must lose oxygen on heating. Between $MnCrO_4$ and $Mn_{1.5}Cr_{1.5}O_4$, intermediate formation of $MnCrO_3$ might be expected. However, this was not confirmed by our experimental XRD data (see Figure S1 in the Supporting Information). Between 400 and 500 °C, evolution of oxygen results in formation of Cr_2O_3 and Mn_3O_4 or their solid solutions. This result seems rather strange because MnO_2 should be stable in this temperature range under oxidizing conditions. On further heating, Cr_2O_3 gradually dissolves in Mn_3O_4 to reduce tetragonal distortion of its spinel-type structure and to form finally the single-phase cubic spinel.

3.3. Static Magnetization and Specific Heat. The temperature dependence of static magnetic susceptibility $\chi = M/B$ in $MnCrO_4$ measured at 0.1 T (Figure 4) exhibits

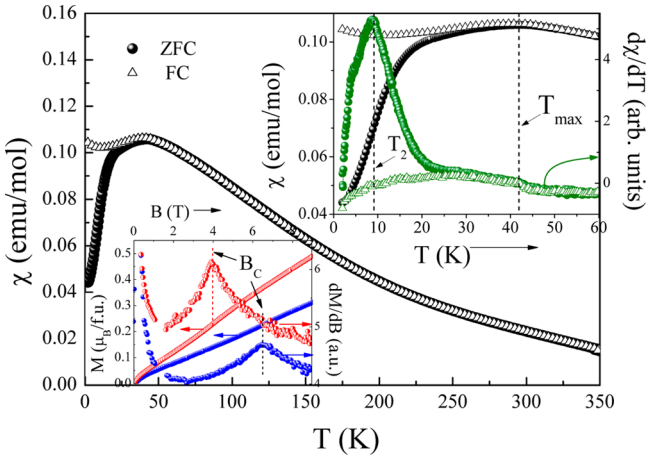

Figure 4. Temperature dependence of the magnetic susceptibility $\chi=M/B$ at B = 0.1 T measured in ZFC (filled circles) and FC (open triangles) regimes. On insets: (right, upper) Enlarged low-T part of $\chi(T)$ and its derivative $d\chi/dT(T)$, indicating the presence of additional anomaly at low temperatures in $MnCrO_4$. (left, lower) Isothermal magnetization curves and the first derivative of the magnetization curves at T = 2 K (blue filled circles) and 5 K (red half-filled circles), revealing an appearance of field-induced anomalies on $M(B)$.

nontrivial behavior at low temperatures. The clearest feature is a rather broad smeared maximum at $T_{max} \approx 42$ K, which appears to indicate either a lower magnetic dimensionality or an order−disorder transition. Below this point the χ drops rapidly both in zero-field cooling (ZFC) and field-cooling (FC) data. In addition, a thorough analysis of $\chi(T)$ in comparison with its derivative $d\chi/dT(T)$ reveals an appearance of additional anomaly at $T_2 \sim 9$ K (see right upper inset in Figure 4). At lowest temperatures, the upturn of χ is seen in FC regime, which can be ascribed to the presence of small amount of impurities in the sample (possibly due to the mixed valence manganese as described below in Sections 3.5 and 3.6). Below T_{max}, one can see also a noticeable divergence between the ZFC and FC magnetic susceptibility data, indicating possible spin-glass-like behavior at low temperatures. In contrast to the case of the recently reported isostructural compound $CuCrO_4$,[4] the $\chi(T)$ vs T plot of $MnCrO_4$, does not follow the Curie−Weiss law up to the highest temperature ($T \approx 350$ K) achieved in our experiments.

dx.doi.org/10.1021/ic401391b | Inorg. Chem. XXXX, XXX, XXX−XXX

The magnetization isotherms $M(B)$ were measured at lowest temperatures and were found to display neither hysteresis nor saturation in magnetic fields up to 9 T (see left lower inset in Figure 4). Within this range of the applied magnetic fields, the magnetic moment is still far below the theoretically expected saturation magnetic moment for Mn^{2+} ($S = 5/2$) $M_S \approx 5\ \mu_B$/Mn atom. A more detailed inspection of the data reveals a slight upward curvature of the magnetization curves. A rather broad but clear maximum is obvious in the derivative dM/dB, which implies a slight left-bending in the $M(B)$ vs T plot (obtained at 2 K) at around 6.5 T (see left lower inset in Figure 4). On raising temperature, the maximum shifts toward lower field side. Supposedly, such features are indicative of a magnetic field induced transition (metamagnetic or spin-reorientation) in $MnCrO_4$. At the same time, the features in dM/dB are very broad. Similarly broad features have been observed in $La_5Ca_8Cu_{24}O_{41}$ in a region of the phase diagram where a long-range antiferromagnetic order is replaced by short-range antiferromagnetic spin correlations.[15]

An approximation of $\chi(T)$ data in terms of a one-dimensional (1D) chain model for $S = 5/2$ spin system[16,17] was found to be unsuccessful. In contrast to the case of the isostructural $S = 1/2$ $CuCrO_4$ compound,[4] therefore, the magnetism of $MnCrO_4$ cannot be described by a 1D AFM chain model.

A direct confirmation for this inference has been obtained from the specific heat data (Figure 5), which at zero magnetic field exhibit a distinct λ-shaped anomaly (centered at $T \approx 42$ K), which is characteristic of a three-dimensional (3D) magnetic order at $T = T_N = 42$ K. In addition, the occurrence of another anomaly at T_2, revealed from the $\chi(T)$ vs T data at ~9 K, is also obvious from the specific heat data (Figure 5).

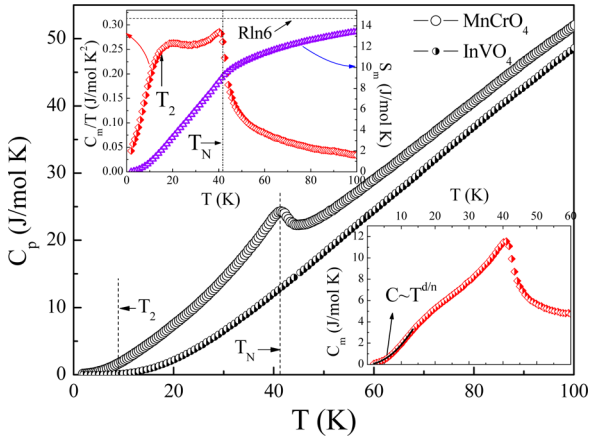

Figure 5. Temperature dependence of the specific heat of $MnCrO_4$ (black open circles) and nonmagnetic isostructural analogue $InVO_4$ (black half-filled circles) at zero magnetic field. The insets show the magnetic specific heat (red half-filled diamonds) and magnetic entropy (blue open triangles) (upper left) and the low-temperature part of magnetic specific heat highlighting the spin wave contribution estimated (black solid curve) (lower right). Arrows indicate two anomalies at T_N and T_2 revealed from the specific heat data.

For quantitative estimations the specific heat data were measured also for nonmagnetic isostructural analogue $InVO_4$. We assume that the specific heat of the isostructural compound $InVO_4$ provides an estimate for the pure lattice contribution to specific heat. The correction to this contribution for $MnCrO_4$ has been made taking into account the difference between the molar masses[18] for each type of atoms in the compound (In−Mn and V−Cr). The values for Debye temperature Θ_D have been estimated as ~338 ± 5 K for the diamagnetic compound $InVO_4$ and ~465 ± 5 K for the $MnCrO_4$. We observe a specific heat jump of $\Delta C_p \approx 12$ J/(mol K) at T_N, which is a bit less than the value predicted from the mean-field theory for the antiferromagnetic spin ordering assuming manganese to be in the high spin Mn^{2+} ($S = 5/2$) state[18]

$$\Delta C_p = 5R\frac{S(S+1)}{S^2 + (S+1)^2} \approx 19.6\ \mathrm{J/(mol\ K)}$$

where R being the gas constant $R = 8.31$ J/(mol K).

The magnetic contribution to the specific heat was determined by subtracting the lattice contribution using the data for the isostructural nonmagnetic analogue $InVO_4$ (see insets in Figure 5). We examine the $C_m(T)$ below T_2 in terms of the spin-wave (SW) approach assuming the limiting low-temperature behavior of the magnetic specific heat should follow $C_m \propto T^{d/n}$ power law for magnons,[19] where d stands for the dimensionality of the magnetic lattice and n is defined as the exponent in the dispersion relation $\omega \approx \kappa^n$. For antiferromagnetic (AFM) and ferromagnetic (FM) magnons, $n = 1$ and $n = 2$, respectively. The least-squares fitting of the data below T_2 (lower inset in Figure 5) has given with good accuracy $d = 2$ and $n = 1.0$ values, that implies presence of 2D AFM magnons at the lowest temperatures. The entropy change has been calculated using the equation: $\Delta S_m(T) = \int_0^T (C_m(T)/T)\,dT$ (upper left inset in Figure 5). One can see that the magnetic entropy ΔS_m almost reaches the saturation value, which is close to those expected from mean-field theory for $S = 5/2$ spin system $\Delta S_{theor} = R\ln(2S+1)$.[18] We note, however, the magnetic entropy released below T_N removes only about 60% of the saturation value. This indicates the presence of appreciable short-range correlations far above T_N, which is usually characteristic feature for materials with lower magnetic dimensionality.[20]

Taking into account that the specific heat data presumes the presence of 2D AFM magnons at the low temperatures we have also tried to analyze the temperature dependence of the magnetic susceptibility in the frame of 2D square lattice model. High-temperature series expansion analysis using the coefficients for $S = 5/2$ spin system[21,22] does not unfortunately give any adequate description of the data. To elucidate further the complex magnetic behavior of new compound $MnCrO_4$, further investigations and theoretical analysis are strongly desirable, preferably on the single crystals.

In applied magnetic fields, the presence of two anomalies ($T_N \approx 42$ K and $T_2 \approx 9$ K) on temperature dependence of the magnetic susceptibility $\chi = M/B$ becomes rather obvious (Figure 6). The position of T_N is almost field-independent up to 9 T, whereas the T_2 anomaly shifts rapidly to lower temperatures with increasing magnetic field. The origin of this T_2 anomaly remains unclear at present.

3.4. Examination of the Magnetic Structure by Density Functional Calculations. We probe the magnetic interactions of $MnCrO_4$ by evaluating the four spin-exchange interactions defined in Figure 7, namely, the two exchanges J_{nn} and J_{nnn} along the edge-sharing chain along the c-direction as well as the interchain exchanges J_1 and J_2. In this investigation, we assume for simplicity that all Mn and Cr atoms are in the +2 and +6 oxidation states, respectively (see below for further discussion). To determine the values of these exchanges, we

dx.doi.org/10.1021/ic401391b | Inorg. Chem. XXXX, XXX, XXX−XXX

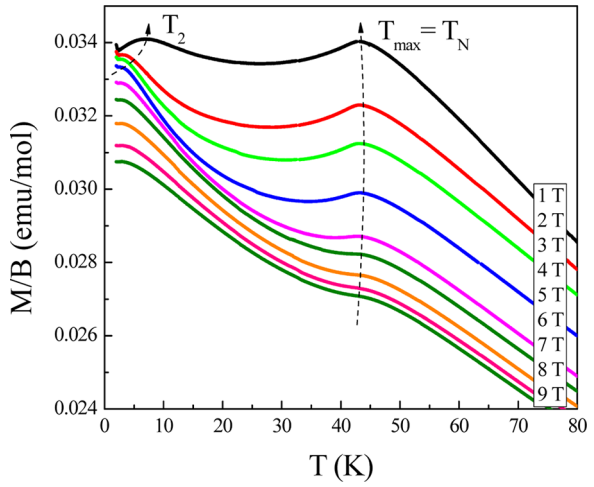

Figure 6. Temperature dependence of the magnetic susceptibility $\chi=M/B$ measured in ZFC regime at various external magnetic fields. For the sake of clarity, the data at 1 and 2 T were shifted on −0.0062 emu/mol and −0.0012 emu/mol, respectively. The dashed lines show the position of the anomalies indicating their shift upon variation of the magnetic field.

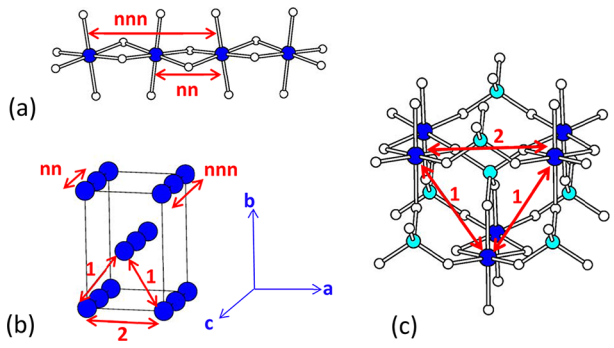

Figure 7. Crystal structure and spin exchange paths in $MnCrO_4$: (a) An isolated MnO_4 chain made up of edge-sharing MnO_6 octahedra, which runs along the *c*-direction. Each MnO_6 octahedron is slightly distorted leading to Mn−O = 2.110 (× 2) and 2.172 (× 4) Å. (b) Arrangement of the Mn^{2+} (S = 5/2) ions in $MnCrO_4$ and the four spin exchange paths J_{nn}, J_{nnn}, J_1, and J_2. (c) Arrangement of MnO_6 octahedra and CrO_4 tetrahedra highlighting the difference between the J_1 and J_2 In a−c, the Mn, Cr and O atoms are indicated by blue, cyan and white circles, respectively. For simplicity, the spin exchange paths J_{nn}, J_{nnn}, J_1, and J_2 are indicated by *nn*, *nnn*, 1, and 2, respectively.

examine the relative energies of the five ordered spin states presented in Figure S2 of the Supporting Information in terms of the Heisenberg spin Hamiltonian

$$\hat{H} = -\sum_{i>j} 2J_{ij}\hat{S}_i\hat{S}_j \quad (1)$$

where J_{ij} (= J_{nn}, J_{nnn}, J_1, J_2) is the exchange parameter for the interaction between the spin sites i and j. Then, according to the energy expressions obtained for spin dimers with N unpaired spins per spin site Mn^{2+}(in the present case, N = 5),[23−25] the total spin exchange energy of each ordered spin state per four formula units (FU) is given as summarized in Figure S2 in the Supporting Information.

We determine the relative energies of the five ordered spin states of $MnCrO_4$ by density functional calculations using the Vienna ab initio simulation package (VASP), the projected augmented-wave (PAW) method,[26] the generalized-gradient approximation (GGA) for the exchange and correlation functional,[27] the plane-wave cutoff energy set to 600 eV, and a set of 4 × 4 × 4 k-point mesh for the Brillouin zone integration. To take into consideration the strong electron correlation associated with the Mn 3d state, we carry out GGA plus on-site repulsion (GGA+U) calculations with U_{eff} = 3, 4, and 5 eV for Mn.[28] The relative energies of the five ordered spin states obtained from our GGA+U calculations are summarized in Figure S2 in the Supporting Information. It should be pointed out that the electronic structures of the five spin ordered states are consistent with the presence of the Mn^{2+} (d^5, S = 5/2) and Cr^{6+} (d^0) ions. We map the relative energies of the five states onto the corresponding relative energies from the total spin-exchange energies,[23] to obtain the values of J_{nn}, J_{nnn}, J_1, and J_2, summarized in Table 3.

Table 3. Spin-Exchange Parameters J_{nn}, J_{nnn}, J_1, and J_2 (in K) of $MnCrO_4$ obtained from GGA+U calculations with U_{eff} = 3, 4, and 5 eV. The last row lists the Curie−Weiss temperature θ (in K) determined from the mean-field-theory approximation using the calculated spin exchanges

	U_{eff} = 3 eV	U_{eff} = 4 eV	U_{eff} = 5 eV
J_{nn}	−2.7	−2.2	−1.9
J_{nnn}	0.1	0.0	0.0
J_1	−2.7	−2.2	−1.8
J_2	−0.1	−0.1	−0.1
θ	−95.4	−77.1	−63.6

Table 3 shows that the magnetic interactions of $MnCrO_4$ are dominated by J_{nn} and J_1, which are both AFM and are essentially identical in strength. J_{nn} is a Mn−O−Mn superexchange (SE), whereas J_1 is a Mn−O···O−Mn super-superexchange (SSE). It is known[24,25] that SSE interactions, often neglected because they are not covered by Goodenough−Kanamori rules,[29] can be stronger than SE interactions. Each high-spin Mn^{2+} (S = 5/2) ion of $MnCrO_4$ has five magnetic orbitals (i.e., all its t_{2g} and e_g orbitals are singly occupied) so that the Mn−O···O−Mn SSE interactions between the edge-sharing octahedral chains can be strong. The oxygen atoms of each MnO_6 octahedron can be classified into the equatorial and axial atoms (O_{eq} and O_{ax}, respectively) with the O_{eq} atoms as the shared oxygen atoms in the edge-sharing octahedral chains. Thus each MnO_6 octahedron has four Mn−O_{eq} bonds and two Mn−O_{ax} bonds. The two adjacent MnO_6 octahedra of the J_1 exchange path are connected by two O_{ax}···O_{eq} contacts, while those of the J_2 exchange path by two O_{eq}···O_{eq} contacts. The Mn−O_{eq} bond is longer than the Mn−O_{ax} bond (2.173 vs 2.110 Å), and the O_{eq}···O_{eq} contact is longer than the O_{ax}···O_{eq} contact (2.752 vs 2.714 Å). This is why J_2 is weaker than J_1. In contrast, each Cu^{2+} (S =1/2) ion of $CuCrO_4$ has only one magnetic orbital contained in the edge-sharing plane, which makes the interchain spin exchange very weak. Thus, the essential magnetic character of $CuCrO_4$ is 1D in nature.

The two dominant spin exchanges J_{nn} and J_1 of $MnCrO_4$ form an essentially 3D cubic AFM lattice in which the 2D square AFM nets (defined by J_{nn} and J_1) parallel to the (110) plane interact antiferromagnetically through J_1. Since J_2 is negligibly weak compared with J_1, the interactions between adjacent 2D square nets are not spin-frustrated. Therefore, $MnCrO_4$ is predicted to undergo a 3D G-type AFM ordering so that the magnetic susceptibility maximum at $T_{max}\approx$ 42 K should be regarded as the Néel temperature T_N, although the χ vs T

dx.doi.org/10.1021/ic401391b | Inorg. Chem. XXXX, XXX, XXX−XXX

plot (Figure 4) around 42 K lacks the characteristic sharp feature expected for a 3D AFM ordering. This interpretation is in agreement with the fact that our specific heat measurements show a λ-anomaly around 42 K. In the mean-field approximation,[30] the Curie–Weiss temperature θ is related to the spin exchange parameters J_{nn} and J_1 as

$$\theta = \frac{2S(S+1)}{3k_B}\sum_i z_i J_i \approx \frac{35(2J_{nn}+4J_1)}{11k_B} \quad (2)$$

where the summation runs over all nearest neighbors of a given spin site, z_i is the number of nearest neighbors connected by the spin exchange parameter J_i, and S is the spin quantum number of each spin site (i.e., $S = 5/2$ in the present case). Therefore, the θ value is estimated to be −95.4, −77.1, and −63.6 K by using the spin exchange constants calculated from the use of U_{eff} = 3, 4, and 5 eV, respectively. These are in reasonable agreement the value of −55 K estimated from the integral ESR intensity, which is a measure of the static magnetic susceptibility (see Section 3.6).

Finally, we examine the reason for the small band gap in $MnCrO_4$ by examining the density of states (DOS) plots calculated for its G-type AFM state (Figure 8). The valence

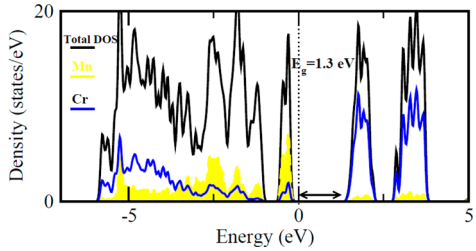

Figure 8. Total DOS plot (black) and projected DOS plots for the Mn 3d (yellow) and Cr 3d (blue) states obtained for the G-type AFM ordered state of $MnCrO_4$ by GGA+U calculations with U_{eff} = 4 eV.

band is dominated by the Mn 3d states, and the conduction band by the Cr 3d states. The band gap E_g is calculated to be 1.3 eV from our GGA+U calculations with U_{eff} = 4 eV. Because E_g is smaller than 1.5 eV, $MnCrO_4$ is expected to be black in color. The reason for the small band gap is that it involves the occupied Mn 3d and the unoccupied Cr 3d states.

3.5. Valence States of Manganese and Chromium and Conduction Properties. It is well-known that chromates (6+) are yellow, and Mn^{2+} compounds are usually colorless or only slightly colored because d-d transitions are forbidden for high-spin d^5 ions. However, our product is black. Before any DOS calculations (Figure 8), this suggested the possibility of partial electron transfer from Mn^{2+} to Cr^{6+}, in accordance with the reducing properties of the former and oxidizing properties of the latter. Consistent with this view, the bond valence sums calculated with the standard bond valence parameters[31] for Mn^{2+} and Cr^{6+} (2.26 and 5.64, respectively) deviate from the integer values as expected, whereas bond valence sums for oxygens are normal (Table 2).

To obtain more detailed information about the charge state of Mn and Cr, we analyzed the experimental XANES data. According to Kunzel's law,[32] with increasing oxidation number, each absorption feature in the XANES spectrum is shifted to higher energies and the energy shifts vary linearly with the valence of the absorbing atom for a given ligand type and coordination. On the other hand, the position of main K edge may vary with ligand type and/or coordination geometry within ~8 eV for Mn[33,34] and up to ~9 eV for Cr.[34,35]

To eliminate the influence of these factors, the reference compounds should have the same chemical environment as do the atoms under study. Therefore, MnC_2O_4*$2H_2O$ (white) and Mn_2O_3 (black) were chosen as standards for Mn^{2+} and Mn^{3+}, and yellow $SrCrO_4$, as a standard for Cr^{6+}.

A theoretical analysis of Mn and Cr K edge experimental spectra was carried out using the coordinates from the XRD study within the nonmuffin-tin approach, the finite difference method (FDMNES 2012).[36] Experimental and theoretical spectra are in good agreement (Figures 9 and 10). Since

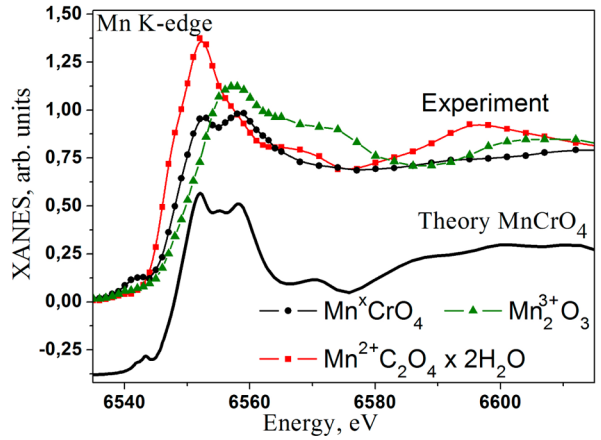

Figure 9. Normalized experimental Mn K-edge XANES spectra for $MnCrO_4$ (black circles), MnC_2O_4·$2H_2O$ (red squares), Mn_2O_3 (green triangles), and theoretical simulation for $MnCrO_4$ (black solid line).

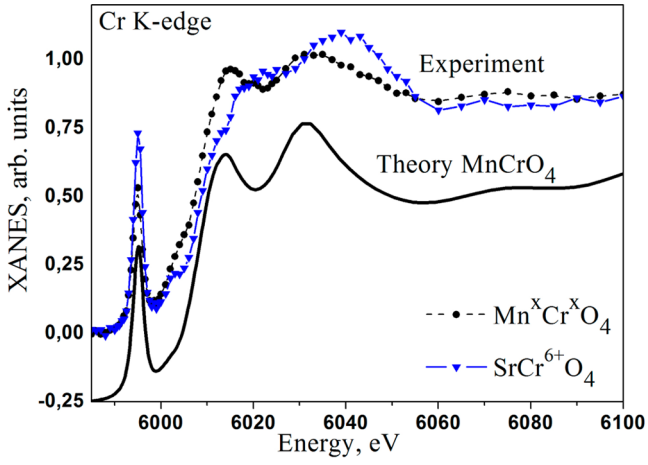

Figure 10. Normalized experimental Cr K-edge XANES spectra for the $MnCrO_4$ (black circles), $SrCrO_4$ (blue triangles), and theoretical simulation for $MnCrO_4$ (black solid line).

XANES is sensitive to the short-range order around absorbing atoms, the crystal structure obtained from XRD correctly predicts the local atomic structure around manganese and chromium atoms.

The energy position of the Mn edge was taken at the inflection point as determined by the first derivative of the absorbance. Such an approach was used in the investigation of the valence states of Mn in mixed-valence manganates,[37] because it generally shows spectroscopic features more clearly than the absorption spectra. Assuming linear relation between

dx.doi.org/10.1021/ic401391b | Inorg. Chem. XXXX, XXX, XXX–XXX

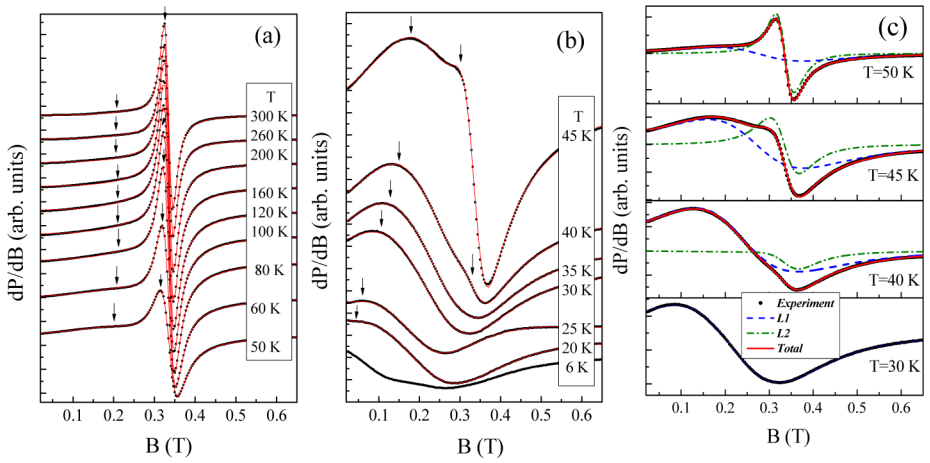

Figure 11. Evolution of the ESR spectra with temperature: (a) high-temperature part, (b) low-temperature part, (c) representative example of the ESR spectrum decomposition along with two resolved absorption lines. The circles are experimental data, and lines are results of fitting according to the Dysonian line shape profile (eq 3).

formal oxidation state and edge energy (not shown here), the Mn oxidation state of $MnCrO_4$ is estimated to be 2.4, in reasonable agreement with the bond valence data.

For chromium, the valence is better defined by the position of the pre-edge feature than by the edge position. The calculations for Cr^{5+} and Cr^{6+} in tetrahedral oxygen environment showed shifting the pre-edge centroid toward higher energies by ~1 eV.[38] The chromium spectra of Figure 10 show a shift of the edge position by ~0.35 eV and that of the pre-edge peak of ~0.3 eV to lower energies with respect to those of the Cr^{6+} oxidation state. This indicates a slightly lower oxidation state of chromium. A numerical estimation cannot be done due to the absence of a suitable reference material for Cr^{5+}, but can be indirectly confirmed through both pre-edge and edge position of the Cr K-edge XANES data of Cr^{5+} and Cr^{6+} in calcium chromates and uranyl compounds containing mixed chromium oxidation states.[39,40]

Additionally, charges on atoms were calculated by means of Bader analysis[41] using the full-potential linearized augmented plane wave method implemented within the Wien2k program package[42] using the GGA PBE exchange correlation potential.[43] Based on the linear correlation between the calculated Bader charges of Mn and Cr atoms and their oxidation states in the reference compounds (see Figure S3 in the Supporting Information), the following oxidation states have been interpolated for Mn and Cr in $MnCrO_4$: 2.85 and 5.45, respectively.

It is evident that all methods used for estimation of the oxidations states are not precise (we have 2.26, 2.4, and 2.85 for Mn, 5.64 and 5.45 for Cr) but all point to considerable charge transfer from Mn^{2+} to Cr^{6+}. Averaged and internally consistent values are 2.5 and 5.5. Additional confirmation of the charge transfer from Mn^{2+} to Cr^{6+} was obtained from the ESR measurements showing two paramagnetic centers with rather different g values (see Section 3.6). In $Mn^{2+}Cr^{6+}O_4$ it would be impossible because Cr^{6+} is diamagnetic.

Mixed-valence compounds usually display considerable electronic conductivity. Measurements done using porous poorly sintered disc resulted in the room-temperature value of 1.4×10^{-5} S/cm with average activation energy of 0.27 eV (see the Supporting Information for details). These values are typical of semiconductors and are consistent with the presence of a mixed-valence state in Mn chains.

It may seem strange that presence of the Jahn–Teller ion, Mn^{3+}, does not result in the characteristic elongation of the MnO_6 octahedron with coordination number (CN) 4 + 2. There are two reasons for this. First, Mn^{3+} is diluted by spherically symmetrical Mn^{2+}. Second, this specific structure type is unfavorable for such elongation, because the axial oxygen, O(1), in contrast to O(2), has only one bond to Mn. Then, bond valence principle demands that Mn–O(1) bond should be shorter than Mn–O(2) bond, resulting in flattened rather than elongated octahedron (CN 2 + 4), or, otherwise, Cr–O bonds should be considerably different in length. The former variant, although rare, does not contradict the Jahn–Teller theorem and takes place in $MnCrO_4$ (see Table 2), whereas the latter takes place in another isomorph with Jahn–Teller ion, $CuCrO_4$.[3,4]

3.6. ESR Study. To further elucidate the complex magnetic properties and valence states of $MnCrO_4$, we have also performed electron spin resonance (ESR) study. The evolution of the ESR spectra of powder sample $MnCrO_4$ with temperature is presented in Figure 11.

The ESR spectra of Figure 11 indicate the presence of two spectral components, a narrow line superimposed over a broad one. The two components exhibit rather different features. The resonance field characterizing the narrow line L_2 varies weakly when the temperature decreases, whereas the broad line L_1 shifts rapidly toward the lower field side below approximately 50 K (see Figure 11b). Similarly, the line width of the broad component manifests the temperature-dependent character in more distinct manner (almost over the whole temperature range investigated) than the narrow one. The results obtained can be understood assuming the existence of two different resonant centers in $MnCrO_4$.

For quantitative analysis of the line shape, each spectrum has been fitted by the sum of two Dysonian line shapes,[44] taking into account a small contribution of the dispersion into absorption. Since the line observed is relatively broad (only one order less than the resonance field value in the present compound), two circular components of the exciting linearly polarized microwave field have to be taken into consideration. Therefore, for a proper analysis, the ESR signals on both sides of $B = 0$ should be included into the fit formula; according to Joshi and Bhat[45]

dx.doi.org/10.1021/ic401391b | Inorg. Chem. XXXX, XXX, XXX–XXX

$$\frac{dp}{dB} \propto \frac{d}{dB}\left[\frac{\Delta B + \alpha(B - B_r)}{\Delta B^2 + (B - B_r)^2} + \frac{\Delta B - \alpha(B + B_r)}{\Delta B^2 + (B + B_r)^2}\right] \quad (3)$$

This describes an asymmetric Lorenzian line, where P is the power absorbed in the ESR experiment, B the magnetic field, B_r the resonance field, and ΔB the line width. α denotes the asymmetry parameter, which is the fraction of the dispersion added to the absorption. The admixture of dispersion to the absorption signal is usually observed in metals. Here, we are dealing with a magnetic semiconductor, in which the asymmetry arises from the influence of nondiagonal elements of the dynamic susceptibility. This effect is often observed in systems with interactions of low symmetry and sufficiently broad resonance lines ($B_r \approx \Delta B$).[46,47]

Results of the ESR line shape fitting by the sum of two asymmetric Lorenzians (eq 3) are shown by red solid lines in Figure 11. An example of the spectrum decomposition along with two resolved lines is given in Figure 11c (blue and green dashed lines are broad and narrow components respectively, while the red solid one is the sum of these lines). The fitted curves are in good agreement with the experimental data. The line width ΔB, the effective g-factor, and the integral ESR intensity (which is proportional to the number of magnetic spins) derived from these fits for the two resolved lines are summarized in Figure 12.

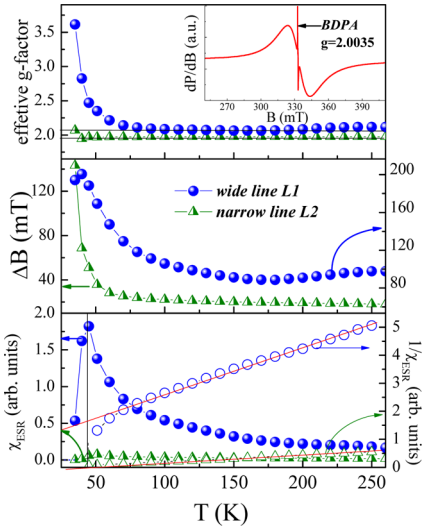

Figure 12. Temperature dependence of the effective g-factor (upper panel), the ESR line width (middle panel) and the ESR susceptibility (i.e., the integrated ESR intensity) along with its inverse value (lower panel) for two resolved ESR lines (circles for L_1 and triangles for L_2). The inset in the upper panel shows the ESR spectrum of $MnCrO_4$ recorded with the reference sample BDPA (g=2.0035).

The effective g-factor was found to be nearly isotropic for both components of the ESR spectra. The average effective g-factors at room temperature are found to be $g_1 = 2.05 \pm 0.03$ for the main (broad) absorption line L_1, and $g_2 = 1.97 \pm 0.01$ for the narrower absorption line L_2. When the temperature decreases, the g_2 remains practically unchanged, while g_1 noticeably grows below ~75 K (the upper part of Figure 12). The line width ΔB_2 varies weakly for the narrow line at high temperatures and demonstrates a rapid increase only below T_N, whereas line L_1 broadens already below ~180 K with decreasing temperature (the middle part of Figure 12). Apparently, such a behavior indicates the presence of strong short-range correlations essentially higher than the ordering temperature T_N, which are frequently characteristic of the systems with lower dimensionality. Similar to the static magnetic susceptibility data presented above, the integral ESR intensity for both ESR signals increases with decreasing temperature, passes through a maximum at about 40−45 K and then decreases (the lower part of Figure 12). At low temperatures (T < 30 K) only one (broad) component L_1 dominates the absorption. Remarkably, this ESR susceptibility $\chi_{ESR}(T)$ for both resolved resonance lines follows the Curie−Weiss relationship at temperatures higher ~50 K with the Curie−Weiss temperature $\theta \approx -55$ K (see Figure 12).

Thus, the ESR data clearly indicate the presence of two different paramagnetic centers in the compound under study. It seems natural to reflect the main (broad) line L_1 ($g_1 \approx 2.05$) to the signal from Mn^{2+}, which play a key role in the magnetic properties of $MnCrO_4$. One can assume that the additional narrow line L_2 ($g_2 \approx 1.97$) in ESR spectra is probably related to a signal due to a small amount of the paramagnetic defect centers that may be associated with the presence of either Cr^{5+} ions or a second phase mentioned in Section 3.1.

5. CONCLUSIONS

The new orthorhombic semiconductive $MnCrO_4$ phase prepared at 400 °C is isostructural to other $M^{2+}Cr^{6+}O_4$ (M = Mg, Co, Ni, Cu, Cd) but differs by partial electron transfer from Mn^{2+} to Cr^{6+}. This is evidenced by Mn and Cr K edge XANES, bond valences and ESR data showing the presence of two different paramagnetic centers with $g_1 \approx 2.05$ and $g_2 \approx 1.97$. Both experimental magnetic susceptibility and specific heat data indicate the occurrence of a 3D AFM order at $T_N \approx 42$ K, which is supported by the spin exchanges evaluated from first principles density functional calculations and by the ESR data. Both static and dynamic magnetic studies indicate the existence of appreciable short-range correlations far above T_N.

■ ASSOCIATED CONTENT

Supporting Information

Crystallographic information file (CIF) and a PDF file containing experimental details and theoretical models. This material is available free of charge via the Internet at http://pubs.acs.org.

■ AUTHOR INFORMATION

Corresponding Author

*E-mail: vbn@sfedu.ru.

Notes

The authors declare no competing financial interest.

■ ACKNOWLEDGMENTS

The authors are thankful to the anonymous referee whose deep insight into the complex magnetic properties of this new material and criticism have brought a new look and forced us to make this work more comprehensive. E.Z. thanks R. Klingeler for useful discussions, T. Vasilchikova for assistance in performing magnetization measurements, and S. Gavrilkin (LPI RAS) for assistance in performing specific heat measurements for $InVO_4$. A.S. thanks J. Liu, J. L. Bettis, Jr., and Professor H. J. Xiang for useful discussions about the mapping analysis, and acknowledges support from SPIN-CNR SEED

project PAQSE001. He also thankfully acknowledges the computer resources from MareNostrum, technical expertise and prompt assistance provided by the Spanish Supercomputing Network (RES) and the Barcelona Supercomputing Center−Centro Nacional de Supercomputación through HPC Grant QCM-2013-1-0048: "MEMOIR: Multiferroic and magnetoElectric Metal OrganIc framewoRks". S.P. and A.S. acknowledge support from the PRIN-2010 Project "Interfacce di ossidi: nuove proprietà emergenti, multifunzionalità e dispositivi per l'elettronica e l'energia (OXIDE)".

REFERENCES

(1) Muller, O.; White, W. B.; Roy, R. *Z. Kristallogr.* **1969**, *130*, 112−120.
(2) Pernet, M.; Quezel, G.; Coing-Boyat, J.; Bertaut, E.-F. *Bull. Soc. Franc. Mineral. Crist.* **1969**, *92*, 264−273.
(3) Seferiadis, N.; Oswald, H. R. *Acta Crystallogr., Sect. C* **1987**, *43*, 10−12.
(4) Law, J. M.; Reuvekamp, P.; Glaum, R.; Lee, C.; Kang, J.; Whangbo, M.-H.; Kremer, R. K. *Phys. Rev. B* **2011**, *84*, 014426.
(5) Chamberland, B. L.; Kafalas, J. A.; Goodenough, J. B. *Inorg. Chem.* **1977**, *16*, 44−46.
(6) Campbell, J. A. *Spectrochim. Acta* **1965**, *21*, 1333−1343.
(7) Kuncewicz, J.; Zabek, P.; Stochel, G.; Stasicka, Z.; Macyk, W. *Catal. Today* **2011**, *161*, 78−83.
(8) Sawamoto, H. *Mater. Res. Bull.* **1973**, *8*, 767−776.
(9) Jang, M.; Weakley, T. J. R.; Doxsee, K. M. *Chem. Mater.* **2001**, *13*, 519−525.
(10) Ammundsen, B.; Paulsen, J.; Davidson, I.; Liu, R.-S.; Shen, C.-H.; Chen, J.-M.; Jang, L.-Y.; Lee, J.-F. *J. Electrochem. Soc.* **2002**, *149*, A431−A436.
(11) Dahn, J. R.; Zheng, T.; Thomas, C. L. *J. Electrochem. Soc.* **1998**, *145*, 851−859.
(12) Larson, A. C.; Von Dreele, R. B. *General Structure Analysis System (GSAS)*; Los Alamos National Laboratory Report LAUR 86−748 ; Los Alamos National Laboratory: Los Alamos, NM, **2004**,.
(13) Toby, B. H. *J. Appl. Crystallogr.* **2001**, *34*, 210−213.
(14) Shannon, R. D. *Acta Crystallogr., Sect. A* **1976**, *32*, 751−767.
(15) Leidl, R.; Klingeler, R.; Büchner, B.; Holtschneider, M.; Selke, W. *Phys. Rev. B* **2006**, *73*, 224415.
(16) Smith, T.; Friedberg, S. A. *Phys. Rev.* **1968**, *176*, 660−665.
(17) Fisher, M. E. *Am. J. Phys.* **1964**, *32*, 343−346.
(18) Tari, A. *The Specific Heat of Matter at Low Temperature*; Imperial College Press: London, 2003.
(19) de Jongh, L. J.; Miedema, A. R. *Adv. Phys.* **1974**, *23*, 1−260.
(20) Carlin, R. L. *Magnetochemistry*; Springer-Verlag: Berlin, 1986.
(21) Lines, M. E. *J. Phys. Chem. Solids* **1970**, *31*, 101−116.
(22) Yamaji, K.; Kondo, J. *J. Phys. Soc. Jpn.* **1973**, *35*, 25−32.
(23) Dai, D.; Whangbo, M.-H. *J. Chem. Phys.* **2001**, *114*, 2887−2893; **2003**, *118*, 29−39.
(24) Whangbo, M.-H.; Koo, H. J.; Dai, D. *J. Solid State Chem.* **2003**, *176*, 417−481.
(25) Xiang, H. J.; Lee, C.; Koo, H.-J.; Gong, X. G.; Whangbo, M.-H. *Dalton Trans.* **2013**, *42*, 823−853.
(26) (a) Kresse, G.; Hafner, J. *Phys. Rev. B* **1993**, *47*, 558−563. (b) Kresse, G.; Furthmüller, J. *Comput. Mater. Sci.* **1996**, *6*, 15−50. (c) Kresse, G.; Furthmüller, J. *Phys. Rev. B* **1996**, *54*, 11169−11186.
(27) Perdew, J. P.; Burke, K.; Ernzerhof, M. *Phys. Rev. Lett.* **1996**, *77*, 3865−3868.
(28) Dudarev, S. L.; Botton, G. A.; Savrasov, S. Y.; Humphreys, C. J.; Sutton, A. P. *Phys. Rev. B* **1998**, *57*, 1505−1509.
(29) Goodenough, J. B. *Magnetism and the Chemical Bond*; Robert E. Krieger Publishing Company: Huntington, NY, 1976.
(30) Smart, J. S. *Effective Field Theory of Magnetism*; Saunders: Philadelphia, 1966.
(31) Brese, N. E.; O'Keeffe, M. *Acta Cryst. B* **1991**, *47*, 192−197.
(32) Mande, C.; Sapre, V. B. In *Advances in X-ray spectroscopy*; Bonnelle, C., Mande, C., Eds.; Pergamon: New York, 1983; Chapter 17, p 287.
(33) Dau, H.; Liebisch, P.; Haumann, M. *Anal. Bioanal. Chem.* **2003**, *376*, 562−583.
(34) Joseph, D., Yadav, A. K., Jha, S. N., Bhattacharyya, D. *Bull. Mater. Sci.* 2013, in press, http://www.ias.ac.in/matersci/forthcoming/Jun13/BOMS-D-12-00324.pdf.
(35) Tromp, M.; Moulin, J.; Reid, G.; Evans, J. *AIP Conference Proceedings* **2007**, *882*, 699−701.
(36) Joly, Y. *J. Synchr. Rad.* **2003**, *10*, 58−63.
(37) Manceau, A.; Marcus, M.; Grangeon, S. *Am. Mineral.* **2012**, *97*, 816−827.
(38) Farges, F. *Phys. Chem. Miner.* **2009**, *36*, 463−481.
(39) Unruh, D.; Quicksall, A.; Pressprich, L.; Stoffer, M.; Qiu, J.; Nuzhdin, K.; Wu, W.; Vyushkova, M.; Burns, P. *J. Solid State Chem.* **2012**, *191*, 162−166.
(40) Arcon, I.; Mirtic, B.; Kodre, A. *J. Am. Ceram. Soc.* **1998**, *81*, 222−224.
(41) Bader, R. F. W. *Chem. Rev.* **1991**, *91*, 893−928.
(42) Blaha, P.; Schwarz, K.; Madsen, G. K. H.; Kvasnicka, D.; Luitz, J. *WIEN2k, An Augmented Plane Wave Plus Local Orbitals Program for Calculating Crystal Properties*; Vienna University of Technology: Vienna, Austria, 2001.
(43) Perdew, J. P.; Burke, K.; Ernzerhof, M. *Phys. Rev. Lett.* **1996**, *77*, 3865−3868.
(44) Dyson, F. *Phys. Rev.* **1955**, *98*, 349−359.
(45) Joshi, J. P.; Bhat, S. V. *J. Magn. Reson.* **2004**, *168*, 284−287.
(46) Benner, H.; Brodehl, M.; Seitz, H.; Wiese, J. *J. Phys. C* **1983**, *16*, 6011−6030.
(47) Krug von Nidda, H.-A.; Svistov, L. E.; Eremin, M. V.; Eremina, R. M.; Loidl, A.; Kataev, V.; Validov, A.; Prokofiev, A.; Aßmus, W. *Phys. Rev. B* **2002**, *65*, 134445.